4 Synthesis and characterization of Na^+ doped system $SrCe_{1-x}Na_xO_3$ (x=0.0,0.02,0.04,0.06 and 0.10)

4.1 Introduction

Extensive studies on high temperature proton conductor (HTPC) materials have been made in the last 20 years. Importance of these materials could make to a fuel cell and other electrochemical applications are widely recognized [215,74,216,15].The most well-known HTPC materials are the perovskite oxides (ABO_3) for example, $BaZrO_3$, $SrZrO_3$, $BaCeO_3$ which were for the first time discovered by Iwahara et al. [13, 217, 218]. Orthorhombic perovskite of strontium cerate ($SrCeO_3$) has been widely studied as proton conductor due to their interesting electrical properties. The conductivities of undoped $SrCeO_3$ is high (2.303×10^{-5} S cm^{-1} at 700 °C) even in hydrogen-containing which limits its application. It is known that doped perovskite- type strontium cerate ($SrCeO_3$) materials exhibit good protonic conductivity at high temperature under a hydrogen-containing atmosphere which could utilize in various electrochemical processes such as hydrogen production, hydrogen sensors, etc. [219, 220].Conventionally, the partial substitution of a trivalent element such as Y^{3+}, Yb^{3+}, Lu^{3+}, Eu^{3+}, and Tm^{3+} for Ce^{4+} is the way to improve proton conductivity of $SrCeO_3$ [196-200,221, 222]. Among them, Yb doped and Y doped systems exhibit 10^{-4}–10^{-3} S cm^{-1} at 400–800 °C and highly suitable for many device applications. Recently composite electrolytes based on $SrCeO_3$ with high ionic conductivities have been explored for the intermediate temperature fuel cells (ITFCs) [201]. Investigation on Novel $SrCe_{1-x}Yb_xO_{3-\alpha}$ (Na/K)Cl composite electrolytes for intermediate temperature solid oxide fuel cells have been carried out [202]. Recently thermal properties of $SrCeO_3$ have been investigated a new thermal barrier coating (TBC) material for applications above 1200 °C. In $SrCeO_3$ di- and tri-valent dopants at Ce sites create oxygen vacancies, $OH^{\cdot}$ occupy these vacant sites and make them proton conductor. However, research reveals that there are still challenges because the conductivity of divalent and trivalent cations-doped $SrCeO_3$ is not high enough to meet the commercial application of solid oxide fuel cells. In the literature, no reports are available on monovalent doped $SrCeO_3$ systems. As

per the charge compensation mechanism doping of monovalent ions at the Ce sites of $SrCeO_3$ will create more oxygen vacancies and hence increase the protonic conductivity. Therefore, in this work, the substitution of Na^{1+} at Ce^{4+} was aimed to achieve improvement in the conductivity by increasing the number of oxygen vacancies.

4.2 Experimental

A few composition of the system $SrCe_{1-x}Na_xO_{3-\delta}$ with x = 0.00, 0.02, 0.04, 0.06 and 0.10, abbreviated respectively as SCN0, SCN2, SCN4, SCN6 and SCN10 have been synthesized by solid state reaction method. $SrCO_3$ (Purity 99.9%, Alfa Aesar), cerium oxide CeO_2, and $Na_2CO_3H_2O$ (Purity 99.5%, Alfa Aesar) were taken as raw materials. Raw material CeO_2 was obtained from the heat treatment of ammonium nitrate $(NH_4)_2Ce(NO_3)_6$ (Purity 99.5%, Alfa Aesar) at 500 °C.

The stoichiometric amounts of $SrCO_3$, CeO_2, and $Na_2CO_3H_2O$ in the presence of acetone (as mixing media) were milled in a planetary ball-mill (PM200, Retsch, Germany) using zirconia balls for 8 h at 200 rpm. The milled powders were subsequently dried in an oven for 12 h. Thermal analysis (TG and DSC) of raw materials and a stoichiometric mixture of raw materials was carried out using simultaneous TG-DSC thermal analyser (Mettler Toledo, Germany), in the temperature range of 30–1000 °C with a heating rate of 10 °C/min in a nitrogen atmosphere. The as-milled powders were calcined in alumina crucible at 1100 °C for 12 h and cooled to the room temperature using a controlled cooling rate. The calcined powders were mixed with 2 wt% polyvinyl alcohol (PVA) and shaped into cylindrical pellets with diameter ~ 12 mm and thickness ~ 2 mm under a load of 5 tons using a hydraulic press. These ceramic pellets were sintered at 1200 °C using a high temperature programmable muffle furnace (Matrix, India). Initially, pellets were heated slowly at a rate of 2 °C/min up to 200 °C and maintained at this temperature for 2 h to ensure the complete burning of the binder. The pellets were then heated at a rate of 5 °C/min to the sintering temperature, 1200 °C and

maintained at this temperature for 12 h then cooled down to the room temperature using a cooling rate 5 °C/min.

The structural phase of these samples was analysed using Rigaku Miniflex II desktop XRD employing Cu-K_α radiation and Ni filter. The room temperature Raman spectrum of the samples was recorded in the wave number range 50–700 cm^{-1} using spectroscope (T64000, Jovin-Yvon Horiba, France). Fourier transform infrared (FTIR) spectrums of the calcined powers were recorded in wave number range 400–4000 cm^{-1} by KBr pellet method using a spectroscope (Shimadzu, Model DF 803, Japan). The UV–Visible spectra in absorption mode of calcined powders have been collected in the range of wavelength 1500–1000 nm by a spectrometer (V-770, Jasco, Japan). Scanning electron micrographs (SEM) and Energy dispersive X-ray spectrum (for compositional analysis) of the fractured surfaces of the sintered pellets were examined using a scanning electron microscope (EVO18, Zeiss, Japan). For the DC resistance measurements, sintered pellets were polished using emery papers of diferent grades. Silver (Ag) paste was applied on both surfaces of the pellet and pellets were cured at 700 °C for 15 min to form silver electrodes. DC electrical resistances were measured using 2-probe method by applying a voltage of 5 V across the pellets from a constant-voltage source using an Electrometer (Model 617, Keithley, USA).

4.3 Results and Discussion

4.3.1 Thermal analysis (TG/DSC) of raw materials and their mixture

Before using raw materials for the synthesis of a few compositions of system $SrCe_{1-x}Na_xO_3$, quality of raw materials was checked by performing thermogravimetric (TG) and differential scanning calorimetry (DSC) analysis. The TGA–DSC curves of raw materials: CeO_2, $SrCO_3$, and $Na_2CO_3H_2O$ were recorded in temperature range 30–1000 °C in a nitrogen atmosphere using heating rate 10 °C/min. The TGA–DSC curves of CeO_2 powder are shown in **Figure 4.1a**. In the temperature range, 30–1000 °C, no significant weight change and endo/exothermic peaks were observed in the TGA and DSC curves of CeO_2 powder confirming high stability and purity of the oxide. The TGA and DSC curves of $SrCO_3$ powder are shown in **Figure 4.1b**. The TGA curve of $SrCO_3$ shows a single step weight loss (27.58%) in the temperature range 850–1000 °C. The observed experimental weight loss may be due to the evolution of CO_2, according to the reaction given below;

$$SrCO_3 \rightarrow SrO + CO_2 \tag{4.1}$$

Theoretical weight loss calculated according to **Eq. (4.1)** is 29.72%, which is slightly higher than the experimental weight loss (27.58%). In the DSC curve of $SrCO_3$, two endothermic reactions peaks cantered at 926 and 977 °C are seen. TGA–DSC curves of $SrCO_3$ were compared with investigations made by Bera et al. [223]. Based on the information available in the literature the first peek (at 926 °C) is assigned to the polymorphic phase transformation of $SrCO_3$ from orthorhombic (space group Pmcn) rhombohedra (space R-3 m), while the second peak (at 977 °C) to the decomposition of $SrCO_3$ into SrO according to reaction (4.1). **Figure 4.1c** shows the TGA and DSC curves of sodium carbonate monohydrate ($NaCO_3H_2O$). The TG curve shows a total weight loss (25.72%) in two steps.

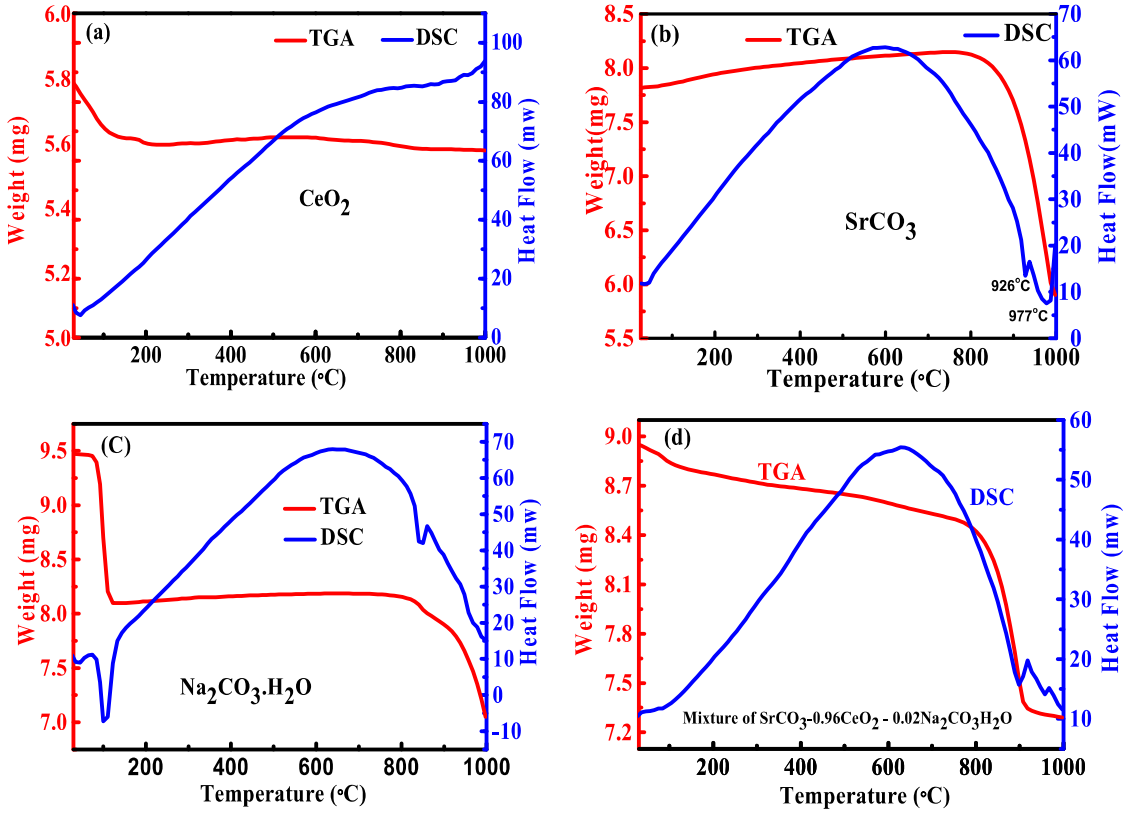

Figure 4.1 Thermo gravimetric analysis (TGA) and differential scanning calorimetric (DSC) curve of raw materials and mixture.

The first step of weight loss (14.52%) is observed in the temperature range 30–125 °C. Theoretical weight loss calculated as per **Eq. (4.2)** given below;

$$Na_2CO_3\,H_2O \rightarrow Na_2CO_3 + H_2O \tag{4.2}$$

The weight loss of 14.50% is the same as the first step experimental weight loss (14.52%). This result indicates that weight loss observed in the temperature range 30–125 °C is due to complete dehydration of $Na_2CO_3H_2O$ into Na_2CO_3 according to **Eq. (4.2)**. The amount of weight loss observed in the temperature range 800–1000 °C is 13.13% which may be due to the decomposition of Na_2CO_3 into Na_2O according to **Eq. (4.3)**;

$$Na_2CO_3 \rightarrow Na_2O + CO_2 \tag{4.3}$$

The theoretical weight loss calculated as per **Eq. (4.3)** is 41.52% much higher than the experimental weight loss in the second step 13.13% this may be due to incomplete conversion of sodium carbonate (Na_2CO_3) into sodium oxide (Na_2O) upto 1000 °C for a heating rate 10 °C/min. Complete decompositions of Na_2CO_3 into Na_2O require temperature > 1000 °C. Due to the limitation of the working temperature of the furnace of the TGA–DSC instrument used in this work, measurement above 1000 °C could not be possible. In the DSC curve of $Na_2CO_3H_2O$ two endothermic peaks at 157 °C and 850.83 °C are seen. The first peak is attributed to the expulsion of water molecules according to **Eq. (4.2)**. The second endothermic peak observed at 850.83 °C is attributed to melting of Na_2CO_3. The melting temperature of Na_2CO_3 reported in the literature is 851 °C [23]. The observed endothermic peak around at 851 °C supports high purity of the sodium carbonate used in this work.

The TGA–DSC curves of ball milled stoichiometric mixture of raw materials for one of the composition $SrCe_{0.96}Na_{0.04}O_3$ are shown in **Figure 4.1d**. The TGA curve shows a small weight loss in the temperature range 30–100 °C, which is assigned to dehydration of $Na_2CO_3H_2O$ to Na_2CO_3. The weight loss (14.25%) observed in the temperature range 800–900 °C may be assigned to the formation of solid solution $SrCe_{0.96}Na_{0.04}O_3$ according to the reaction given below;

$$SrCO_3 + 0.96CeO_2 + 0.02Na_2CO_3 + 0.03O_2 \rightarrow SrCe_{0.96}Na_{0.04}O_3 + 1.02CO_2 \quad (4.4)$$

The weight loss of 13.92% observed experimentally agrees with the theoretical weight loss calculated according to the reaction (4.4). Constant weight in the temperature range 900–1000 °C confirmed that all-important thermal events had been completed. DSC curve shows only one endothermic peak between 800 and 900 °C. This peak is attributed to solid state reaction among raw materials to form $SrCe_{0.96}Na_{0.04}O_3$ (SCN4). Based on the results of the thermal analysis of raw materials and mixture, it was decided to synthesize all powders by fixing calcination temperature 1100 °C and time 12 h. Various techniques have characterized

the synthesized powders, and results of these investigations are described in subsequent sections.

4.3.2 Phase analysis and structural characterization

Room temperature powder X-ray diffraction (XRD) patterns of the synthesized compositions of system $SrCe_{1-x}Na_xO_3$ are displayed in **Figure 4.2 (a)**. X-ray diffraction pattern of the samples was indexed using JCPDS (Card No. 47-1689) file available in the literature for $SrCeO_3$ with orthorhombic structure and space group Pnma. Absence of any X-ray diffraction peaks corresponding to raw materials and secondary phase confirms that synthesized Na doped $SrCeO_3$ solid solutions are single phase material. To ensure incorporation of Na at Ce site of $SrCeO_3$, magnified view of the highest intensity peak corresponding to (112) refection plane is obtained and shown in **Figure 4.2 (b)**. The position of this peak shifts towards lower angle side up to composition with x=0.04 (SCN4).On further increase in the concentration of dopant Na, a reversal trend (towards higher angle side) is seen. The shift in the position of XRD peaks on doping is noticed depending on the difference in the ionic radius of the dopant and host. It is known that the probabilities of substitution at A or B site in perovskite oxides, ABO_3 depends on the valence state and ionic radii corresponding to the coordination number (CN) of the dopant ion and the substituted site-ion. In perovskite oxide $SrCeO_3$, the coordination number of Sr is twelve while of Ce is six. Ionic radius of the Ce^{4+} and Na^{1+} ion in 6-fold co-ordination number is 0.87 and 1.02 Å, respectively. In 12-fold co-ordination number, the ionic radius of Sr^{2+} ion and Na^{1+} ion is 1.42 and 1.39 Å, respectively. The peak shift towards lower angle side for the composition with x = 0.02 (SCN2) and 0.04 (SCN4) indicates that Na^{1+} is substituted at Ce^{4+} of $SrCeO_3$. For the remaining compositions with x = 0.06 (SCN6) and 0.10 (SCN10) reversal in the peaks shift direction may possible if Na^{1+} substitutes at Sr^{2+} site instead of Ce^{4+}.

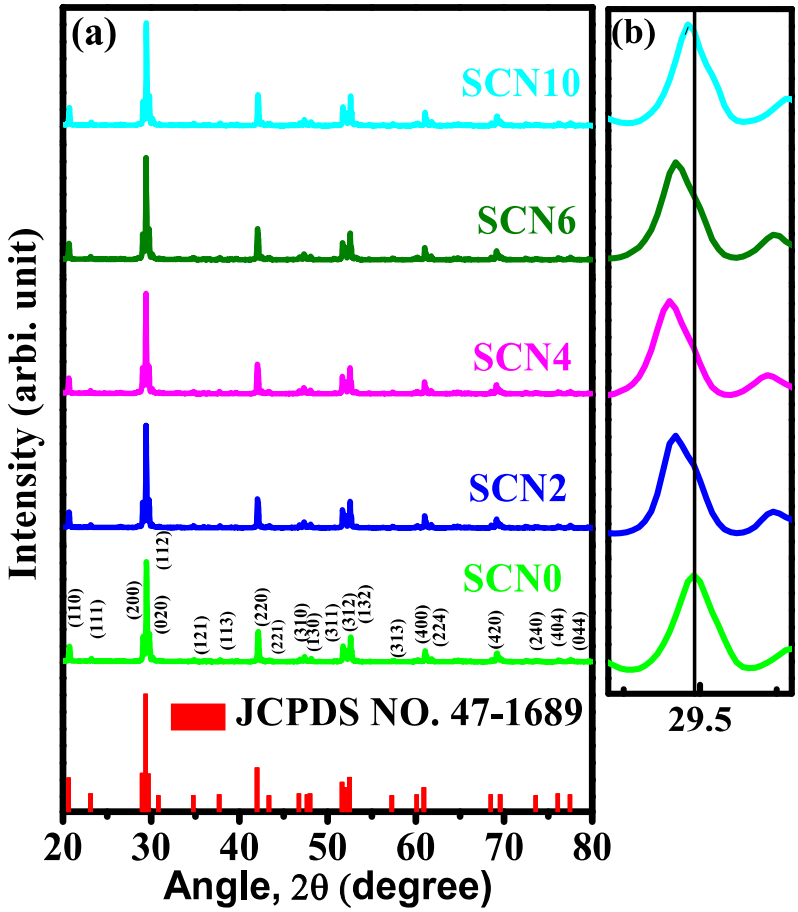

Figure 4.2 (a) Room temperature X-ray diffraction (XRD) and **(b)** magnified view of (112) peak of the samples.

The ionic radius of Sr^{2+} in 12-fold coordination number is 1.44 Å while of Na^{1+} is 1.39 Å. The difference in the ionic radius and valency of Sr^{2+} and Na^{1+} is smaller than that of Ce^{4+} and Na^{1+}. The XRD results of Na doped samples can be interpreted that in compositions with x = 0.02 (SCN2) and 0.04 (SCN4), Na^{1+} ions preferentially substitute at Ce^{4+} sites, in composition with x = 0.06 (SCN6) distributed between the Sr^{2+} and Ce^{4+} sites and in composition with x = 0.10 (SCN10) completely on the Sr^{2+} sites. Sharing of particular dopants between A and B sites in perovskite oxides has been reported. In fact, dopants Nd^{3+} and Gd^{3+}

at Ce^{4+} site of $SrCeO_3$ have shown preference for the Sr site at the dilute limit and "Amphoteric" behaviour with partitioning over both Sr and Ce sites [224].

Structural parameters for all the samples were obtained by Rietveld refinement using FullProf Suite software package. Structural refinement was carried out using the space group Pnma and distorted orthorhombic structure of $SrCeO_3$ phase [206]. The patterns were refined for lattice parameters, scale factor, backgrounds, pseudo-Voigt profile function (u, v and w), atomic coordinates, and overall isothermal temperature factors (Biso). **Figure 4.3 (a)** shows the observed, calculated, and the difference in XRD patterns. There is a good fitting between the observed and calculated patterns, which indicates that substitution of Na^{1+} at Ce^{4+} site of $SrCeO_3$ has not induced any structural transition. The value of lattice parameters selected bond angles, and length, along with reliability factors, are given in Table 4.1. The crystal structure of all the compositions was modelled by VESTA program using the Rietveld refined structural parameters, and the typical crystal structure of one of the sample SCN4 (x = 0.04) is shown in **Figure 4.3 (b)**. The average crystallite size of the calcined powder of all the samples was determined from high intense Bragg's peak corresponding to (112) refection using Scherrer's equation

$$D = \frac{k\lambda}{\beta \cos\theta_{max}} \tag{4.5}$$

Where D- crystallite size, k is the Scherrer's constant = 0.9 for spherical particles, λ is the wavelength of X-ray, β is the full width at half maximum (FWHM) of diffraction peak after subtracting the instrumental line broadening in radians, and θ is the Bragg's diffraction angle. The calculated average crystallite size for all the samples are listed in Table 4.1.

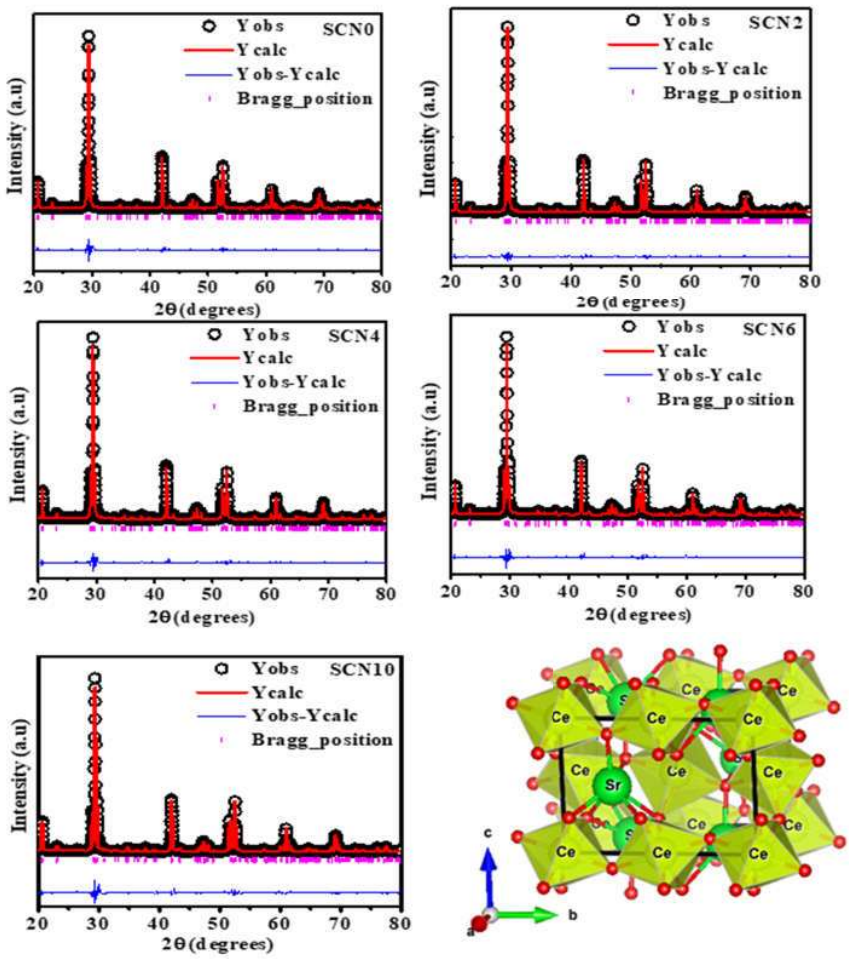

Figure 4.3 (a) Rietveld refinement XRD profile of the samples and **(b)** Crystal structure of the sample SCN4 (x=0.04) obtained using VESTA.

The crystallite size calculated using Debye-Scherrer's method is not considered to be accurate because the line broadening may also have a contribution due to microstrain. In the literature Size Strain Plot (SSP) method has been used to evaluate the crystallite size and microstrain. The advantage of this method is that it gives less weightage to the data of reflection arises from higher angles where precession is lower. Therefore, Size Strain Plot (SSP) method has been used to determine the crystallite size and microstrain the samples. As per the SSP plot method, interplanar spacing and microstrain is related according to **Eq. (4.6)**;

$$\left(\frac{d_{hkl}\beta cos\theta}{\lambda}\right)^2 = \frac{k\lambda}{D}\left(\frac{d_{hkl}^2\beta cos\theta}{\lambda^2}\right) \quad (4.6)$$

Table 4.1 Structural parameters obtained from Rietveld refinement analysis of XRD data of the samples.

$SrCeO_3$ Space Group: Pnma (62) (orthorhombic)	**SrCeO3 (SCN0)**	**$SrCe_{0.98}Na_{0.02}O_3$ (SCN2)**	**$SrCe_{0.96}Na_{0.04}O_3$ (SCN4)**	**$SrCe_{0.94}Na_{0.06}O_3$ (SCN6)**	**$SrCe_{0.90}Na_{0.10}O_3$ (SCN10)**
Lattice Parameters(Å)	a = 6.1483 b = 8.5826 c = 6.0085	a = 6.1497 b = 8.5834 c = 6.0091	a = 6.1516 b = 8.5864 c = 6.0110	a = 6.1486 b = 8.5820 c = 6.0080	a = 6.1489 b = 8.5828 c = 6.0081
Cell Volume($Å^3$)	317.06	317.19	317.50Å	317.03	317.07
Atomic Coordinates	**Occupancy**				
Sr (4c)	0.5017	0.5008	0.5012	0.4998	0.4915
Ce (4b)	0.5014	0.4903	0.4811	0.4695	0.4501
Na (4b)	0.0000	0.0087	0.0192	0.0290	0.0485
OI (4c)	0.5064	0.5044	0.4999	0.4967	0.4889
OII (8d)	1.0026	1.0021	1.0028	1.0030	1.0023
Bond length(Å)					
	2.6908	2.6461	2.6091	2.6791	2.6656
Ce-OI	2.2945	2.2945	2.2522	2.2801	2.3146
Ce-OII	3.5273	3.6150	3.6201	3.5419	3.5756
Sr-OI	2.8526	2.8527	2.8577	2.8415	2.8681
Sr-OII					
Bond angle(°)					
	69.2878	68.7115	67.6587	69.3509	68.6821
OII-Ce-OI	118.906	119.443	121.580	119.389	119.0932
OI-OII-Sr	38.6583	39.3988	39.0776	40.8912	39.3460
OI-OII-OII					
Reliability Factors :	R_P = 4.7 R_{wp} = 4.3 χ^2 = 1.33	R_P = 4.8 R_{wp} = 4.5 χ^2 = 1.96	R_P = 4.6 R_{wp} = 4.4 χ^2 = 1.75	R_P = 4.6 R_{wp} = 4.1 χ^2 = 1.33	R_P = 4.2 R_{wp} = 4.6 χ^2 = 1.43

Where, d_{hkl} is the interplanar spacing corresponding to the plane (hkl), k, λ, and D are the same as mentioned in **Eq (4.5)** and ε is the average strain generated in the lattice. The plot of $\left(\frac{d_{hkl}\beta cos\theta}{\lambda}\right)^2$ vs.$\left(\frac{d_{hkl}^2\beta cos\theta}{\lambda^2}\right)$for all the samples are shown in **Figure 4.4**. By linear fitting of the experimental data points, the value of slope and intercept were obtained. The value of crystalline size is determined by value of the slope. Square root of the intercept on y-axis provides the value of lattice strain. The values of crystallite size and lattice strain of various

compositions are given in Table 4.2. Slightly higher value of crystallite size obtained from SSP plot method than Debye Scherrer's method is due to inclusion lattice strain contribution in SSP method. Further, it is observed that the crystallite size of Na doped samples is higher than undoped samples. On the other hand, lattice strain is highest for the undoped sample $SrCeO_3$. It is obvious from Table 4.2 that lattice strain is inversely proportional to the crystallite size.

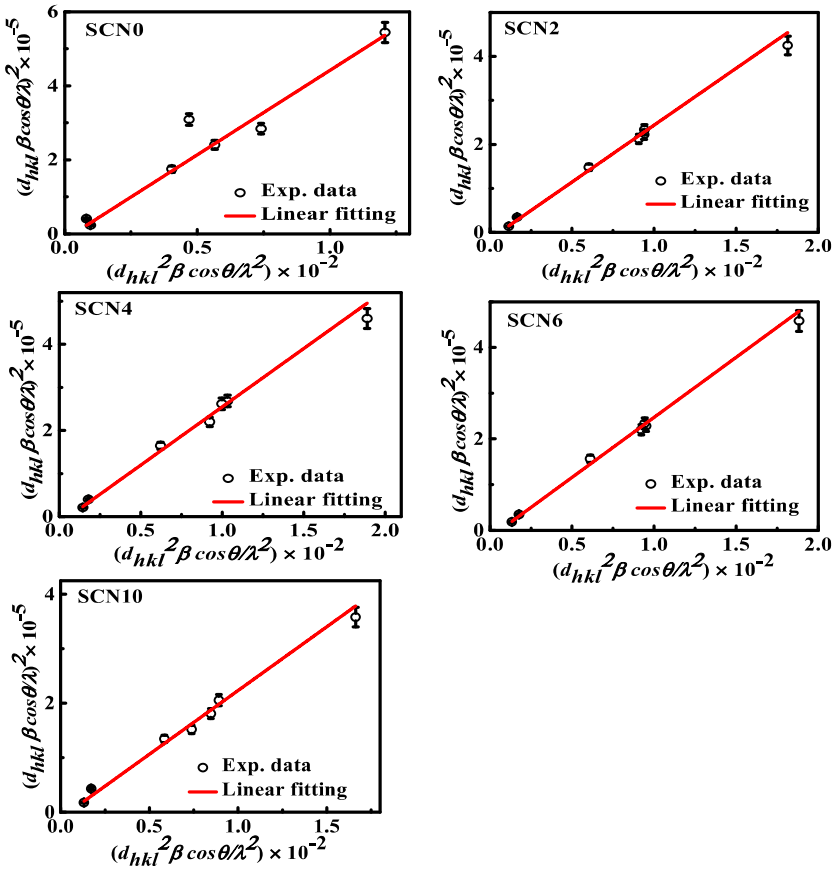

Figure 4.4 Size strain plots (SSP) for the determination of crystallite size and lattice strain of samples.

Table 4.2 Crystallite size, lattice strain determined from size strain plots (SSP) method and optical band gap from Tauc plots of the samples.

Sample Code	Crystallite size (nm)		Lattice strain (ε)x10^{-4}	Optical band Gap (eV)	
	Debye-Scherrer	SSP		Direct	Indirect
$SrCeO_3$(SCN0)	55.6	58.0	14.30	3.01	2.30
$SrCe_{0.98}Na_{0.02}O_3$(SCN2)	59.2	60.1	5.58	3.11	2.42
$SrCe_{0.96}Na_{0.04}O_3$(SCN4)	59.8	62.4	2.57	3.14	2.43
$SrCe_{0.94}Na_{0.06}O_3$(SCN6)	58.2	60.2	3.74	3.08	2.41
$SrCe_{0.90}Na_{0.10}O_3$(SCN10)	58.1	61.5	5.00	2.94	2.32

4.3.3 Raman spectra analysis

It has been reported that the presence of impurity phases such as Sr_2CeO_4, $SrCO_3$ and CeO_2 in trace amount is unavoidable in the powder of $SrCeO_3$ synthesized by any methods. Synthesizing hundred percent pure phase powder of $SrCeO_3$ is challenging even till date. Detection of the impurity phase Sr_2CeO_4 using XRD technique is difficult because of the similarity in the XRD pattern of $SrCeO_3$ and Sr_2CeO_4. It has been noticed from the literature survey that the Raman spectra of $SrCeO_3$ and Sr_2CeO_4 is completely different.

Moreover, Raman spectroscopy can detect lower concentrations of impurity phases and is more sensitive than XRD. Therefore, to check the purity of the synthesized powders, room temperature Raman spectra in the wave number range 50-700 cm^{-1} has been recorded and shown in **Figure 4.5 (a)**.The most intense Raman band in the spectrumof all samples appears at 339.51 cm^{-1}.Other than this intense band two satellite bands at 369.46 and 313.36 cm^{-1} are also seen in the spectrum of all the samples. The spectrum and position of various bands observed for $SrCeO_3$ (SCN0) synthesized in this work are in agreement with the Raman spectra recorded by earlier workers [225]. This result confirms the formation of high purity powder of $SrCeO_3$.

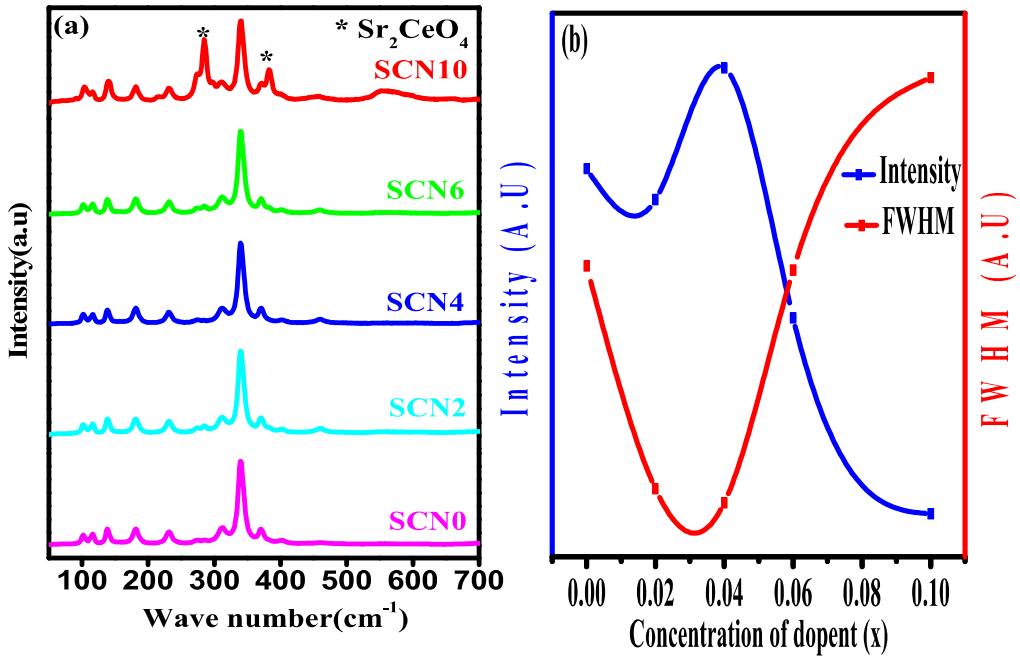

Figure 4.5 (a) Room temperature Raman spectra of all samples and **(b)** Variation of intensity and full width at half maxima with concentration of dopant Na (x).

The Raman spectrum of Na-doped samples (SCN2, SCN4, SCN6, and SCN10) is similar to undoped sample $SrCeO_3$ (SCN0), indicating that the crystal structure of these Na doped samples remains unchanged even on the increasing concentration of Na up to 10 mole %. The highest intensity band (observed at 339.51 cm^{-1}) in the Raman spectra of all the samples is assigned to Ce-O stretching vibration mode associated with the CeO_6, octahedral. Since the Ce^{4+} ion occupies a centrosymmetric site in the structure of $SrCeO_3$, the Raman-active Ce-O vibrational modes involve motions of the oxygen ions only [226]. On substitution of Na^{1+}asmallshift in the position (1.5 cm^{-1}) of this band towards lower wavelength side has been noticed for the compositions with x = 0.02 (SCN2) and 0.04 (SCN4). For the other two compositions x=0.06 (SCN6) and 0.10 (SCN10) position of the band stays unchanged. Almost negligible change in the position of the most intense band even for the highest concentration x=0.10 (SCN10) is surprising because the difference in the atomic mass of host Ce (140 A.U.)

and dopant Na (23A.U.) is large. However, it is mentioned above that this band corresponds to symmetric stretching of CeO_2 band in which only O atoms move, therefore the frequency of this mode may not depend on the difference in the atomic mass of substituent (Na) and host (Ce). Similar results have been reported for rare earth metals and Ca-doped CeO_2 system [227].

On the other hand, a systematic, measurable change in the intensity and full width at half maxima (FWHM) of the band (as shown in **Figure 4.5 (b)** is seen. The intensity of the band is highest, and FWHM is lowest for the composition with x=0.04 (SCN4) which confirms the least distorted/defective structure of this sample in agreement with XRD results. In the Raman spectra of composition with x = 0.10 a few extra modes are seen (marked with * in **Figure 4.5 (a)**) assigned to Sr_2CeO_4 phase. XRD result has shown that in the composition with x=0.10 (SCN10) most of the Na^{1+} ions occupy Sr^{2+} sites. When Na^{1+} ions occupy Sr^{2+} sites instead of designated Ce^{4+}sites, the formation of Sr-rich phase (Sr_2CeO_4) is possible. Due to similar XRD pattern of Sr_2CeO_4 and $SrCeO_3$, XRD could not be able to detect this phase. Another reason is that the amount of Sr_2CeO_4 phase may be below the detection limit of the XRD.

4.3.4 Fourier Transform Infrared (FTIR) Analysis

It is mentioned above that powders of $SrCeO_3$ have impurity phase $SrCO_3$ due to its high stability. Fourier Transform Infrared technique is the most sensitive technique for the detection of impurities based on alkaline earth carbonates is shown in **Figure 4.6**. This technique can detect a concentration of $\leq 0.6\%$ of alkaline earth carbonates. Therefore, to detect the presence of strontium carbonate ($SrCO_3$) in the synthesized powders, the FTIR spectrum of the samples has been recorded and shown in **Figure 4.6**. The FTIR spectrum of undoped sample $SrCeO_3$ (SCN0) is in agreement with earlier reports [228].

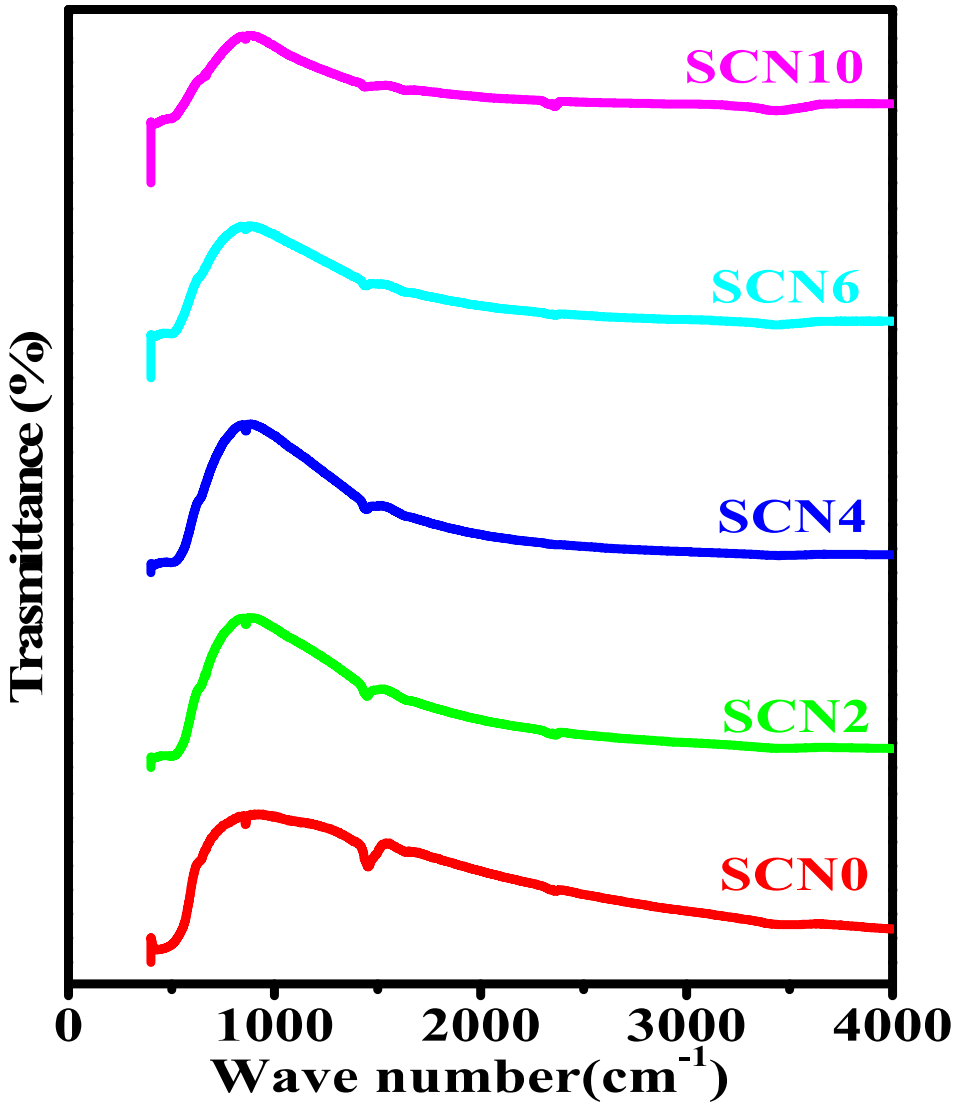

Figure 4.6 Fourier Transform Infra-red (FTIR) spectra of the samples**.**

The FTIR spectrum of Na doped samples is also similar to the undoped sample. In the spectrum of all the samples, incomplete broadband below 500 $cm^{-1}$is observed which is assigned to Ce-O vibration in CeO_6 octahedra. Two weak intensity bands observed at 860 and 1453 cm^{-1}in the spectrum of few samples can be assigned to C-O vibration due to unavoidable traces of $SrCO_3$. This result is contradictory to the result obtained by XRD (**Figure 4.2**) and

Raman studies in which no reflection peaks and modes were seen corresponding to $SrCO_3$ phase. Another weak intensity band observed at 2361 cm^{-1}suggestspresence of CO_2 gas in the chamber of FTIR spectrometer [229]. It is possible that the formation of $SrCO_3$ in the samples have taken place during the experiment by adsorbing CO_2 on the surface of samples.

4.3.5 UV-Visible Spectra Analysis

To determine the optical band gap of the synthesized samples, UV–Vis spectra in absorbance mode is recorded in the wavelength range 100-1000 nm, as shown in **Figure 4.7**. There is a strong absorption band below 400 nm in the spectrum of all the samples. On substitution of Na^{1+}, the position of the absorption maxima shift towards higher wavelength side up to x=0.04 (SCN4) and after that shifted towards lower wavelength side on further increase in the concentration. The optical absorbance's data are shown in **Figure 4.7** were taken to form a Tauc plot by using the Tauc equation given below;

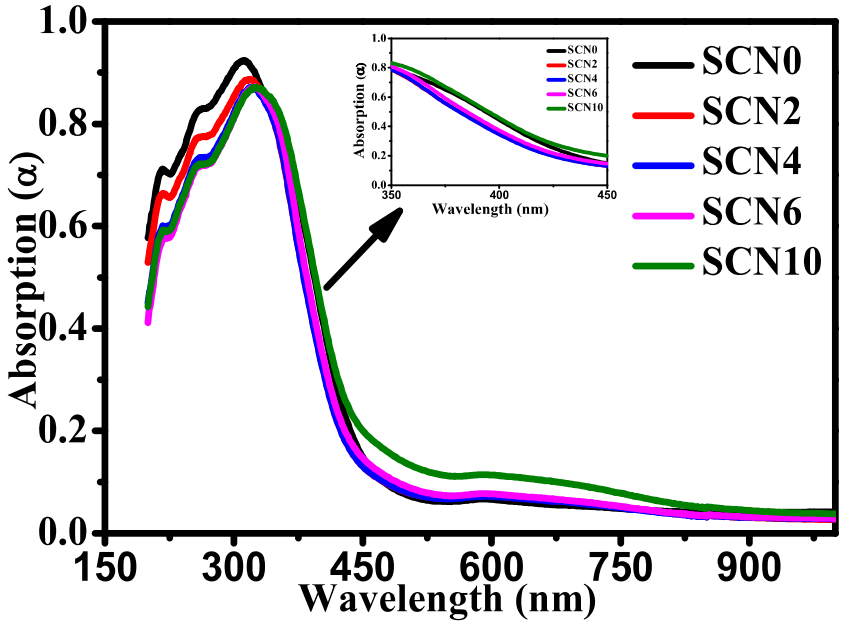

Figure 4.7 Room temperature UV-visible absorption spectra of the samples.

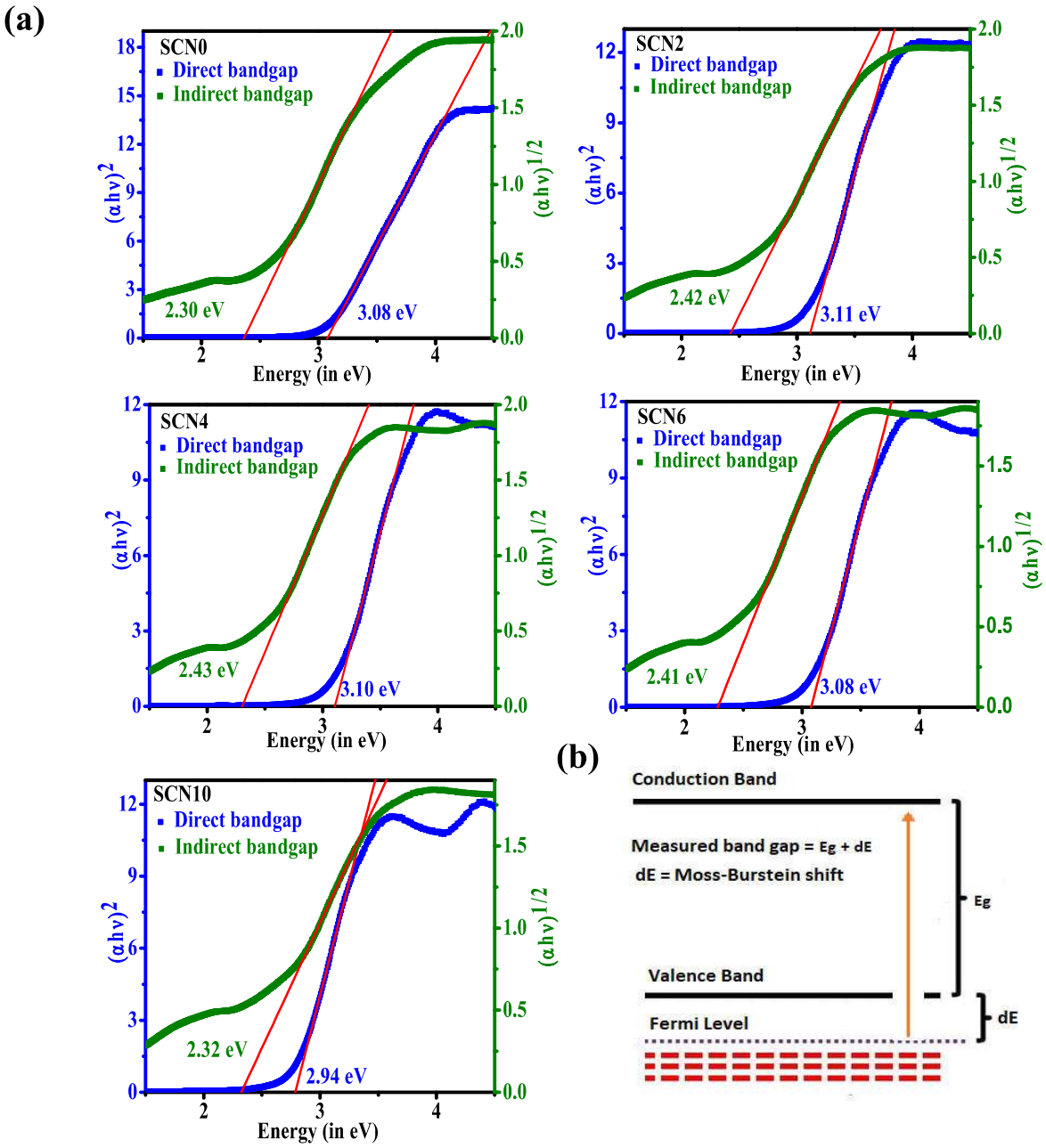

Figure 4.8 (a) Tauc plots obtained from the absorption data of the samples **(b)** Proposed change in the optical band gap of $SrCeO_3$ on Na doping.

$$(ahv)^{1/n} = A(hv - E_g) \quad (4.7)$$

Here α is the absorption coefficient, h is the Planck's constant, ν is the photon frequency, A is the constant, and E_g is the optical band gap energy. The value of exponent n represents the nature of the optical transitions, n = ½ and 2 denotes the direct and indirect allowed transitions, respectively. The band gap values are determined from the linear fitting at the inflection point of $(ahv)^{1/n}$ versus hv plots. The obtained abscissa (hv) intercepts correspond to the optical band gap values. Tauc plots for both direct and indirect transitions for all the samples are shown in **Figure 4.8 (a)**. Obtained values of the direct and indirect band gap of all the samples are presented in Table 4.2 .From Table 4.2; it is noted that the direct band gap for $SrCeO_3$ is 3.01 eV and the indirect band gap is 2.31 eV. The obtained value of the direct band gap of $SrCeO_3$ is lower than the theoretical and experimental value of the band gap by reported earlier workers. Other than this report, no data were reported in the literature concerning the optical gap of $SrCeO_3$. The value of the direct band gap of Na doped samples is higher than the undoped samples. The highest value of band gap E_g = 3.14 eV is observed for sample with x=0.04 (SCN4) and the lowest band gap Eg = 2.94 eV for the sample with x=0.10 (SCN10). Increase in the value of the energy band gap on Na doping can be explained based on the Burstein–Moss shift effect. According to this effect in p-type degenerate semiconductors, the Fermi level can be located in the valance band (**Figure 4.8 (b)** right bottom). In this case, the optical transitions of an electron from valence band can take place only to the energy levels in the conduction band from those levels which are below the Fermi level. Therefore, the location of self-absorption edge shifts towards higher energy, and thus, E+dE would be the effective optical band gap. Reason for p-type degenerate semiconductors of the Na doped samples will be explained in section 1.24.7 (electrical conduction).

It is noted from Table 4.2 that value of indirect bandgap is lower than the value of direct band gap of the same composition. Indirect transitions in wide band ceramic oxides are

observed due to the presence of band corresponding to defects such as oxygen vacancies (V_o^x , $V_o^{\bullet}$ and $V_o^{\bullet\bullet}$), lattice defects and distortion in local bond. The most commonly found defects in oxides materials are oxygen vacancies (V_o^x, $V_o^{\bullet}$ and $V_o^{\bullet\bullet}$) which may generate on account of sintering (at 1200 ^oC) and to compensate charge imbalance. Furthermore, it is noticed that value of the indirect band gap (see Table 4.2) remains almost same for all the doped samples.

4.3.6 Microstructural studies

For the electrical characterization calcined powder of all the compositions were pelletized and sintered at 1200 °C for 12 h. To establish a correlation between microstructure and conductivity, microstructural characterization of fractured surfaces of sintered pellets was made by employing scanning electron microscope (SEM), images are shown in **Figure 4.9**. A clear cut change in the morphology and grain size is noticed with increasing concentration of Na content (x). Grains of samples with x=0.00 (SCN0) and 0.02 (SCN2) have smooth edges and spherical. SEM of samples with x=0.04 (SCN4), 0.06 (SCN6), and 0.10 (SCN10) exhibits well-developed grains and grain boundaries. Closed pores at grain boundaries are also seen in the micrographs. To determine the average grain size, a histogram of the distribution in grain size of all the samples was obtained using Image J software. By fitting the Gaussian function to these histograms (**Figure 4.10**) average grain size of the samples is obtained and presented in Table 4.3. It is noticed from Table 3 that as the concentration of Na dopant increases, the average grain size increases upto x =0.04 (SCN4) after that grain size has decreased on further increased in the Na content. The value of average grain size is smallest for undoped, while the largest for the sample with x=0.04 (SCN4). Increase in the grain may be associated with the formation of a small fraction of the liquid phase during the sintering process promoted by the Na additions. No exaggerated grain growth has been observed in any Na doped samples. From the microstructural studies, it is inferred that density Na doped samples are higher than that of the undoped sample. To confirm its experimental density (d_{exp}) of the sintered pellets was

determined using Archimedes' principle. The theoretical density (d_{th}) of the samples was calculated from the molecular weight of the samples and their lattice parameters obtained by the Rietveld analysis. The percentage porosity of the ceramic of the samples is calculated using the formula;

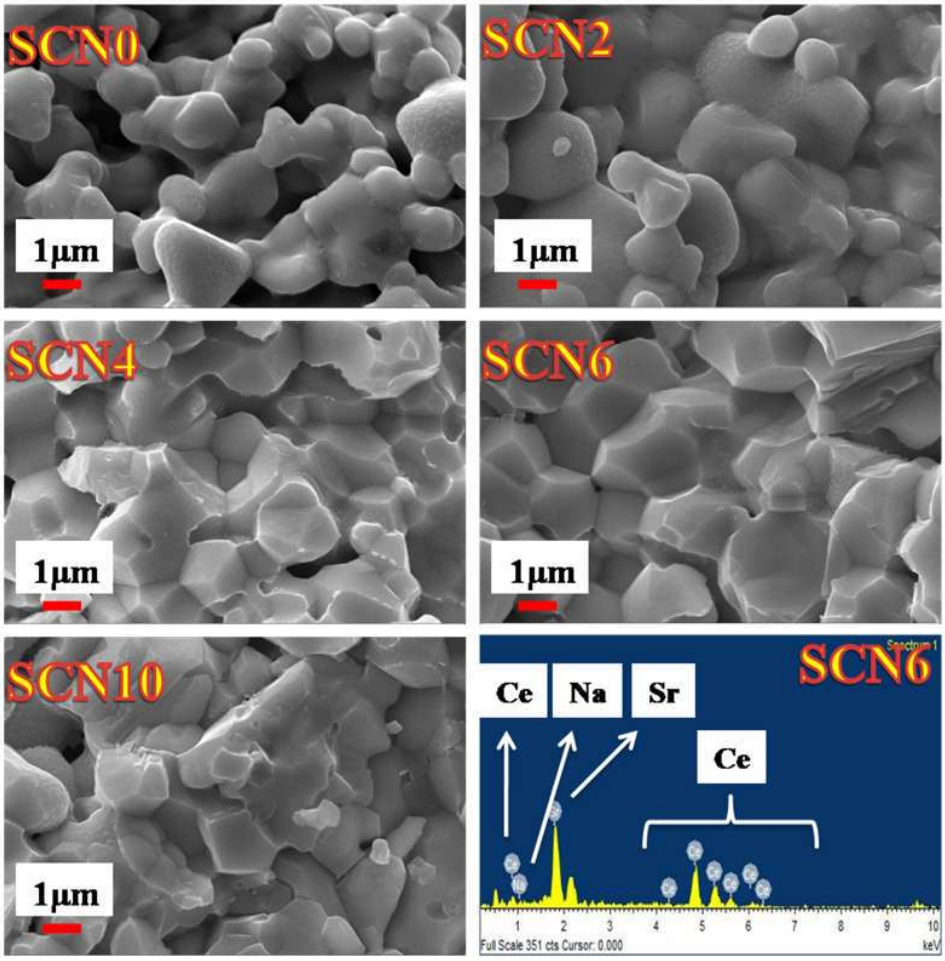

Figure 4.9 Scanning electron micrographs (SEM) of fractured surfaces of the samples and EDXA spectrum of SCN6.

$$\%\, porosity = \frac{[d_{th} - d_{exp}]}{d_{th}} \times 100 \quad (4.8)$$

The value of percentage porosity of all the samples is mentioned in Table 4.3. It is noticed from Table 4.3 that the experimental density of all Na doped samples is higher that undoped samples. The lowest amount of porosity (3 %) is present in the sample with x=0.04 (SCN4) whereas the highest (7 %) in the undoped sample (SCN0). It is worthwhile to mention that in this work, all the samples have been synthesized under the same processing parameters.

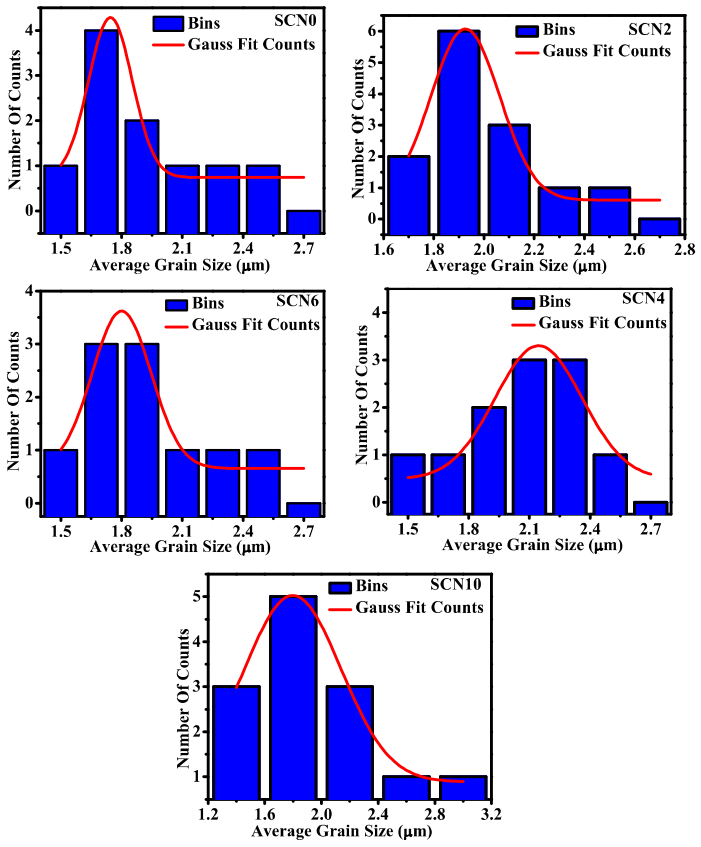

Figure 4.10 Histograms of the distribution of grain size of the samples.

4.3.7 Electrical measurements

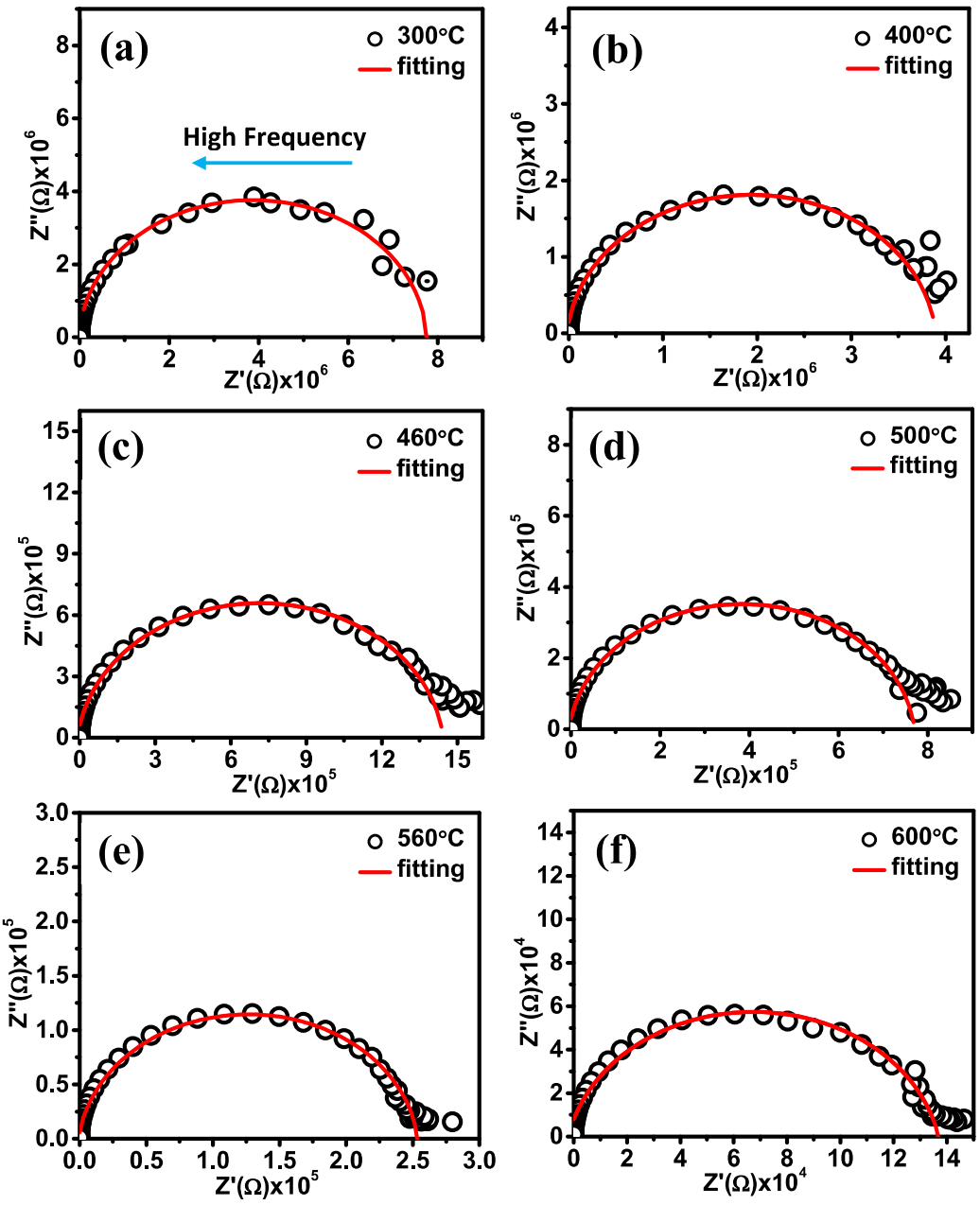

Figure 4.11 The complex plane impedance plots at different temperatures for the composition SCN10.

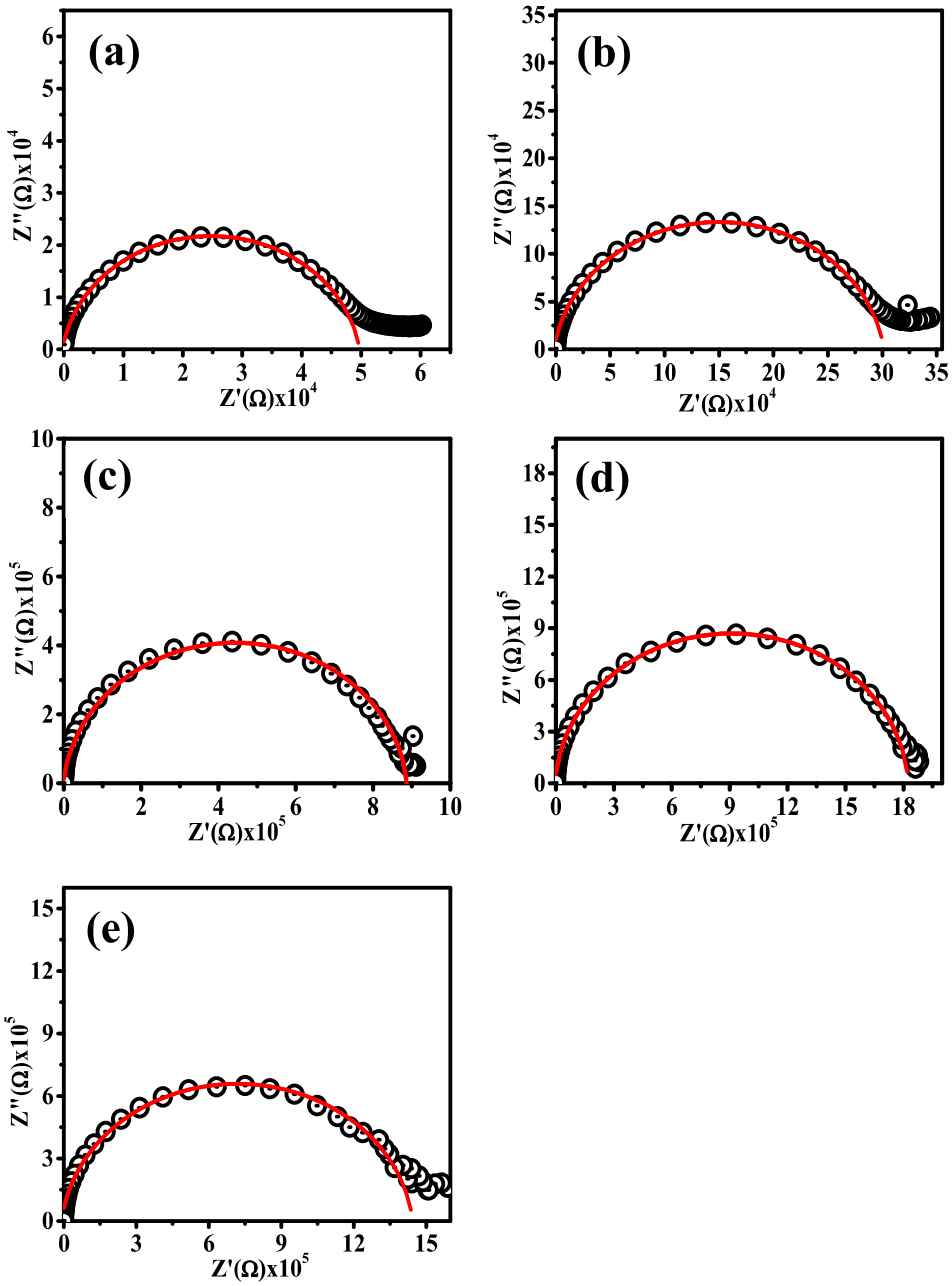

Figure 4.12 The complex plane impedance plots for compositions: **(a)** SCN0 **(b)** SCN2, **(c)** SCN4 **(d)** SCN6 **(e)** SCN10 for $SrCe_{1-x}Na_xO_3$ ($0.00 \leq x \leq 0.10$): at 460 °C.

Impedance spectroscopy (IS) is an effective and simple tool to study the electrical properties of the polycrystalline materials. It facilitates the tailoring of polycrystalline materials by separating the contribution of different parts i.e. grain, grain-boundary and electrode-specimen interface to the electrical conductivity [230]. Thus, this tool is applied to analyze the effect of Na doping on the electrical property of $SrCeO_3$. To study the evolution of impedance with temperature, the complex plane impedance plots were drawn at different temperatures for all samples. As a representative sample, complex impedance plots for sample SCN10 at different temperatures with nonlinear curve fitting are shown in **Figure 4.11(a)-(e)**. From the above figures, one can observe that a part of one depressed semi-circular arc appears at 300 °C which grew with the increase of temperature with a tendency to complete this arc. With further increase in temperature, again a part of a depressed semi-circular arc with a tail at one end appeared. The reason behind this nature of impedance spectra is a decrease in relaxation time of different contributions with an increase in temperature. The value of the resistance of the semi-circular arc was obtained by non-linear curve fitting method. The capacitance corresponding to observed circular arc was calculated by relation $2\pi fRC = 1$ where f, R, and C are peak frequency, resistance, and capacitance which hold good at peak of the corresponding semi-circular arc. The capacitance is found to be in the order of nF. Initially, it shows that the observed semi-circular arc represents the contribution of grain boundaries. But, there may be another possibility that observed semi-circular arc is due to the combined contribution of grains and grains boundaries both.

To show the variation of impedance for all compositions, typical complex plane impedance plots with nonlinear curve fitting for each composition are shown in **Figure 4.12 (a)-(e)** at 460 °C. The above figure indicates that the sample SCN0 has the lowest impedance. Here, the total resistance, R corresponding to both contributions can be obtained from the intercept of the depressed semi-circular arc on the real axis.

Total DC resistances (R) of the samples were measured in the temperature range 300-600 °C using 2- probe method. The corresponding total DC conductivity (σ_{dc}) has been calculated using the formula:

$$\sigma_{dc} = (1/R) \times (L/S) \quad (4.9)$$

Where L is the thickness and S is the surface area of the sample. The plot of the log σ_{dc} versus the inverse of temperature (1000/T) of all the samples is shown in **Figure 4.13**. The linear plot of logσ_{dc} with 1000/T shows that the conductivity follows the Arrhenius relation, given by

Table 4.3 Values of average grain size, % porosity, DC conductivity and activation energy, of the samples.

Sample	**Average grain size (µm)**	**% Porosity**	**DC conductivity (log σ_{dc}) at 600°C**	**Activation Energy (eV)**
$SrCeO_3$(SCN0)	1.72	6.98	-4.10	1.03
$SrCe_{0.98}Na_{0.02}O_3$(SCN2)	1.93	5.98	-5.27	0.86
$SrCe_{0.96}Na_{0.04}O_3$(SCN4)	2.15	4.10	-5.21	0.87
$SrCe_{0.94}Na_{0.06}O_3$(SCN6)	1.87	5.43	-4.86	0.79
$SrCe_{0.90}Na_{0.10}O_3$(SCN10)	1.81	5.79	-4.71	0.92

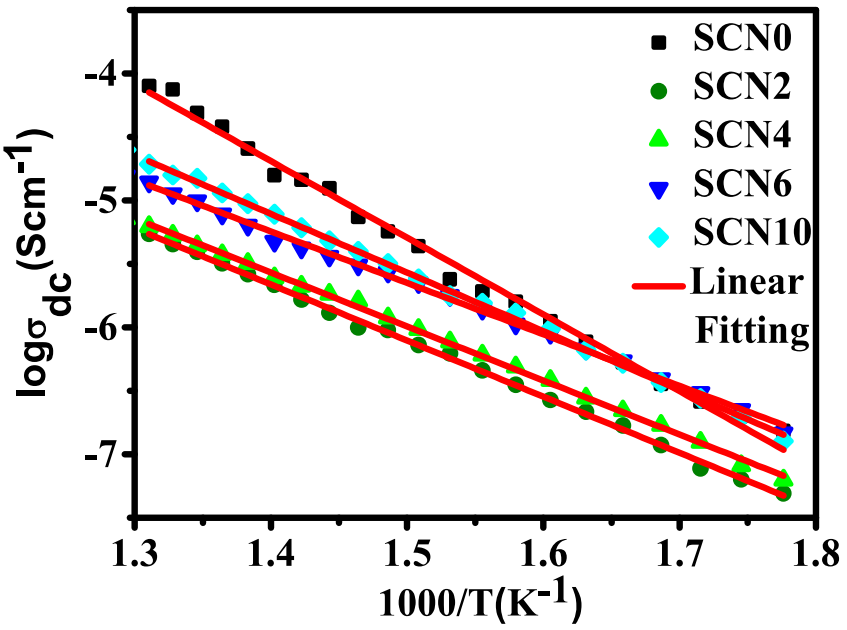

Figure 4.13 DC conductivity for various compositions SCN0, SCN2, SCN4, SCN6 and SCN10 of the system $SrCe_{1-x}Na_xO_3$.

$$\sigma_{dc} = \sigma_o exp(-E_a/K_B T) \quad (4.10)$$

Where σ_0 – pre-exponential factor, k_B – Boltzmann's constant, T is absolute temperature, and E_a is the activation energy for the conduction. Values of activation energy of DC conduction (E_a) for all the samples determined from the least square fitting of the data shown in **Figure 4.13** are given in Table 4.3. The determined values of the activation energy lie in the range of activation energy predicted for the migration of doubly-ionized oxygen vacancies (Vö) in perovskite oxides [231]. Value of the activation energy (Ea) for sample SrCeO3 (SCN0) is 1.03 eV. It is worthwhile to mention here that samples in this work have been synthesized at high temperature (1200 °C) and in air. At this temperature oxygen ions may leave the lattice by generating oxygen vacancies and electrons;

$$O_o^{\times} \rightarrow V_O^{\cdot\cdot} + 2e' + \frac{1}{2}O_2(g) \quad (4.11)$$

The possible charge compensation mechanism on substitution of Na^{1+} ions at Ce^{4+} sites of $SrCeO_3$, according to Kröger–Vink notation can be represented by equations ;

$$Na_2O + 2CeO_2 = 2Na'''_{Ce} + 6h^{\cdot} + 5O_O \quad (4.12)$$

$$Na_2O + CeO_2 = 2Na'''_{Ce} + 3V_O^{\cdot\cdot} + 3O_O \quad (4.13)$$

That is either by generation of electronic holes ($h^{\cdot}$) or oxygen vacancies ($Vo^{\cdot\cdot}$). In Y^{3+} doped $SrCeO_3$ system $SrCe_{1-x}Y_xO_3$, charge compensation by the generation of oxygen vacancies (**Eq. 4.12**) had been supported by Raman scattering measurements. An additional mode at 640 cm^{-1} with increasing intensity on increasing doping concentration (x) was observed in the Raman spectra of the samples [232]. Unfortunately, in the Raman spectra of Na doped samples synthesized in this work, no additional mode around 640 cm^{-1} is seen (**Figure 4.5**). Absence of Raman mode corresponding to the generation of oxygen vacancies of Na doped samples suggests that the charge compensation mechanism in Na^{1+} doped samples is not by the creation of oxygen vacancies. It is well known that Na is a volatile element and in this work, samples have been synthesized at 1200 °C, therefore, doping mole percentage in the samples may be less than the nominal mole percentage. In many acceptor doped perovskites systems, mechanism of charge compensation (electronic or ionic) depends on the concentration of the dopants (x). Further, it is reported that K^{1+} and Na^{1+} substituted at Sr^{2+} sites of $SrTiO_3$ have shown p-type conductivity due to the formation of electron holes. Increase in the value of optical band gap of $SrCeO_3$ on Na-doping (Table 4.2) also supports electronic charge compensation mechanism in the samples, according to **Eq (4.11)**. Doping of one Na^{1+} ion at Ce^{4+} will generate three holes, due to a large number of holes, Fermi level will move within the Valance band, hence increase in the optical band gap is observed. Na-doped samples have also been synthesized at high temperature; therefore, generation of oxygen vacancies and electronic defect according to **Eq (4.10)** is also possible. The expression for the total conductivity of Na-doped samples can be given by;

$$\sigma_{total} = \sigma_i + \sigma_p + \sigma_h = 2e[V_o^{\cdot\cdot}]\mu_{V_O} + en\mu_e + ep\mu_p \quad (4.14)$$

According to data available in Table 4.3, both activation energy and conductivity (at 600 °C) of Na-doped samples are lower than the undoped sample (SCN0). The lower values of the activation energy of Na doped samples than the undoped sample (SCN0) may be due to the formation of dipole defect viz; [2(NaCe)‴ - 3Vo¨]. Strong bonding between these two defects will allow only short-range migration of oxygen vacancies. The activation energy required for the long-range migration of oxygen vacancies is also higher than short-range migration. Three possible reasons for the decrease in value of the activation energy and conductivity on Na doping are; (i) decrease in the mobility of oxygen vacancies and (ii) decrease in the number of electrons (e′) on recombining with holes (h˙) and (iii) change in the microstructure. Conductivity depends on the microstructure structure; also the grain size of $SrCeO_3$ is smaller than the grain size of Na doped samples.

Therefore, the role of grain boundaries will be more in $SrCeO_3$ as compared to Na doped samples. Generally, the activation energy for migration of charges in grain boundaries is higher than within the grains. The higher value of the activation of $SrCeO_3$ (SCN0) suggests that the role of grain boundaries in electrical conduction is more as compared to doped samples. In a similar system, $Ba_{1-x}Na_xCeO_3$ also decreases in the value of conductivity on increasing Na concentration had been reported [33].Values of the conductivity of the samples reported in this work are comparable to the literature values of the conductivity of $SrCeO_3$ (5.13×10^{-7} $S \cdot cm^{-1}$ at 500 °C and 2.09×10^{-5} $S \cdot cm^{-1}$ at 700 °C) [234]. Generally, decrease in the value of the activation energy leads to the increase in the conductivity but Na doped samples, decrease in the value of conductivity and activation simultaneously is surprising and understanding the actual reason for the decrease more studies are needed.

4.3.8 X-ray Photoelectron Spectroscopy (XPS) analysis

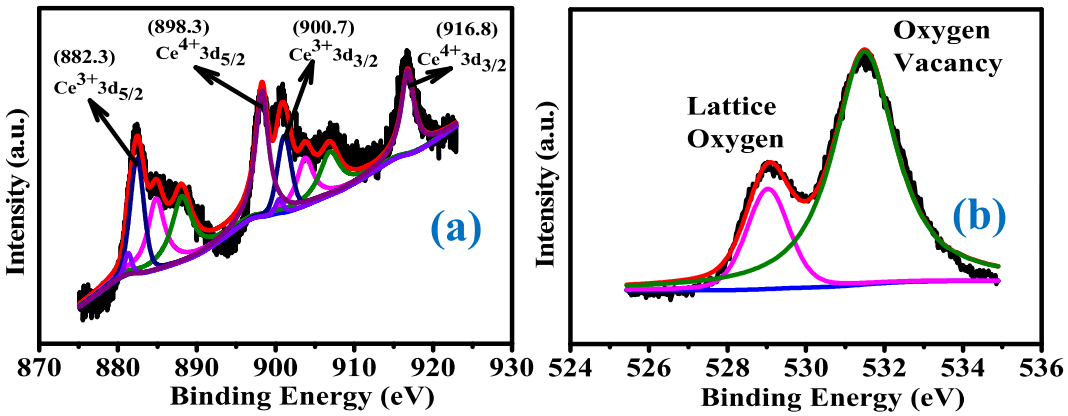

Figure 4.14 (a) Deconvoluted XPS of Ce 3d profile of sample $SrCe_{0.96}Na_{0.04}O_3$ (SCN4) **(b)** Deconvoluted XPS of O 1s profile.

To determine the valence states of constituents elements presents in SCN4 composition, X-ray photoelectron spectroscopic technique has been carried out. The valance states of various elements are determined from the High-resolution XPS spectrum (HRXPS) for each element. **Figure 4.14 (a)** depicts the HRXPS spectrum for Ce. The peaks observed at particular binding energies were matched with binding energy value for Ce^{3+} and Ce^{4+} reported in the literature [235]. Presence of the peaks of Ce^{4+} $3d_{3/2}$ (916.8), Ce^{4+} $3d_{5/2}$ (898.3), Ce^{3+} $3d_{3/2}$ (900.7) and Ce^{3+} $3d_{5/2}$ (882.3) for sample SCN4 has obviously showed existence of Ce in both Ce^{3+} and Ce^{4+} states.

Figure 4.13 (b) displays the XPS spectrum of O 1*s*; two peaks at 529.10 eV and 531.45 eV. The lower binding energy (529.10 eV) peak is associated with lattice oxygen, whereas the higher binding energy (531.45 eV) normally corresponds to oxygen vacancies [236]

4.4 Conclusions

Single phase powder of Na doped $SrCeO_3$ samples was successfully synthesized using a solid state reaction method. X-ray diffraction studies have confirmed Amphoteric nature (sharing of between Sr and Ce sites) of dopant Na in $SrCeO_3$. Crystal structure and space group of all the synthesized samples are the same, i.e., orthorhombic and Pnma. Raman spectra of undoped and doped samples are the same ruling out any major structural change in $SrCeO_3$ on Na doping. FTIR spectroscopic analysis has indicated that as Na concentration increases the formation of $SrCeO_3$ decreases. UV-visible spectra in absorption mode have confirmed that the optical band gap of Na doped samples is higher than the undoped sample. The increase in the value of optical band gap has been explained based on the Burstein-Moss effect. Microstructural studies confirmed that grain size increases with increasing Na concentration. This is account based on the low melting point of Na_2CO_3 aiding sintering. Values of activation energy for DC conduction and conductivity at 600 ^oC of Na doped samples are lower than that of the undoped sample. The decrease in the value of the activation on Na doping is explained in term of restriction in the mobility of oxygen vacancies due to defect pair formation or due to a decrease in several electronic charge carriers.